# Imaging "Invisible" Dopant Atoms in Semiconductor Nanocrystals

Aloysius A. Gunawan,[†] K. Andre Mkhoyan,*[,†] Andrew W. Wills,[‡] Malcolm G. Thomas,[§] and David J. Norris*[,‖]

[†]Department of Chemical Engineering and Materials Science and [‡]Department of Chemistry, University of Minnesota, Minneapolis, Minnesota 55455, United States

[§]Cornell Center for Materials Research, Cornell University, Ithaca, New York 14853, United States

[‖]Optical Materials Engineering Laboratory, ETH Zurich, Zurich, Switzerland

Ⓢ *Supporting Information*

ABSTRACT: Nanometer-scale semiconductors that contain a few intentionally added impurity atoms can provide new opportunities for controlling electronic properties. However, since the physics of these materials depends strongly on the exact arrangement of the impurities, or dopants, inside the structure, and many impurities of interest cannot be observed with currently available imaging techniques, new methods are needed to determine their location. We combine electron energy loss spectroscopy with annular dark-field scanning transmission electron microscopy (ADF-STEM) to image individual Mn impurities inside ZnSe nanocrystals. While Mn is invisible to conventional ADF-STEM in this host, our experiments and detailed simulations show consistent detection of Mn. Thus, a general path is demonstrated for atomic-scale imaging and identification of individual dopants in a variety of semiconductor nanostructures.

KEYWORDS: *Electron energy loss spectroscopy, annular dark-field scanning transmission electron microscopy, colloidal quantum dots, semiconductor nanocrystals, dopant imaging, solotronics*
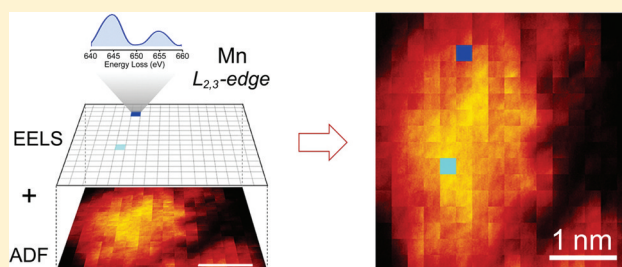
Electronic devices have long relied on the intentional incorporation of impurities, or dopants, to control semiconducting materials. As the size of these devices shrinks, nanometer-scale volumes of semiconductor can contain only a few impurity atoms,[1] presenting new possibilities for doped nanostructures.[2] In particular, solotronic devices now aim to exploit solitary dopants in a semiconductor to obtain new electronic, magnetic, and optical capabilities. However, in doped nanostructures, statistical fluctuations in the number and position of the impurities can have a dramatic effect on the overall behavior.[3] Thus, the ability to locate the dopants through atomic-scale visualization is often critical for understanding the physics of these materials. For example, identification of the lattice sites of dopant atoms in lightly doped complex oxide thin films can lead to an understanding of the unusual transport behavior.[4,5]

Visualization could also address difficulties in the preparation of doped nanostructures. For example, colloidal quantum dots are chemically synthesized, nanometer-scale crystals of semiconductor that exhibit optical spectra that can be tuned with size,[6] an effect that is useful for many applications.[7−9] To control the optoelectronic properties of these materials further, researchers have worked to incorporate impurities. Doped nanocrystals also allow solotronic behavior to be studied in extremely small volumes.[10−13] However, while some progress has been made in the synthesis of doped nanocrystals,[14−16] the preparation of many systems remains a challenge. To test

different approaches, it would be helpful if the number and location of the dopants could be observed directly.

Only a few techniques allow imaging of a single dopant within a semiconductor. Atom-probe tomography creates such images by disassembling a material via field emission and detecting the type and origin of the ejected atoms. However, because the sample must be shaped as a tip to obtain the necessary electric field, this approach is best suited to nanostructures with a high aspect ratio (e.g., nanowires[17]). For nanocrystals, which are roughly spherical in shape, it is more challenging to apply. Another technique, scanning transmission electron microscopy (STEM), has potential to be more broadly applicable, especially with the resolution achievable with aberration-correction.[18−20] A highly focused electron beam is scanned across the sample while scattered electrons are collected with an annular dark-field (ADF) detector. This allows high-resolution images with atomic-number (Z) contrast to be obtained. Indeed, single dopants within a crystalline semiconductor have been imaged with the ADF-STEM approach.[21−23] An atomic column that contains an impurity appears with slightly different contrast in the image. However, despite its success this approach suffers from a fundamental limitation. The dopant must have a large Z-
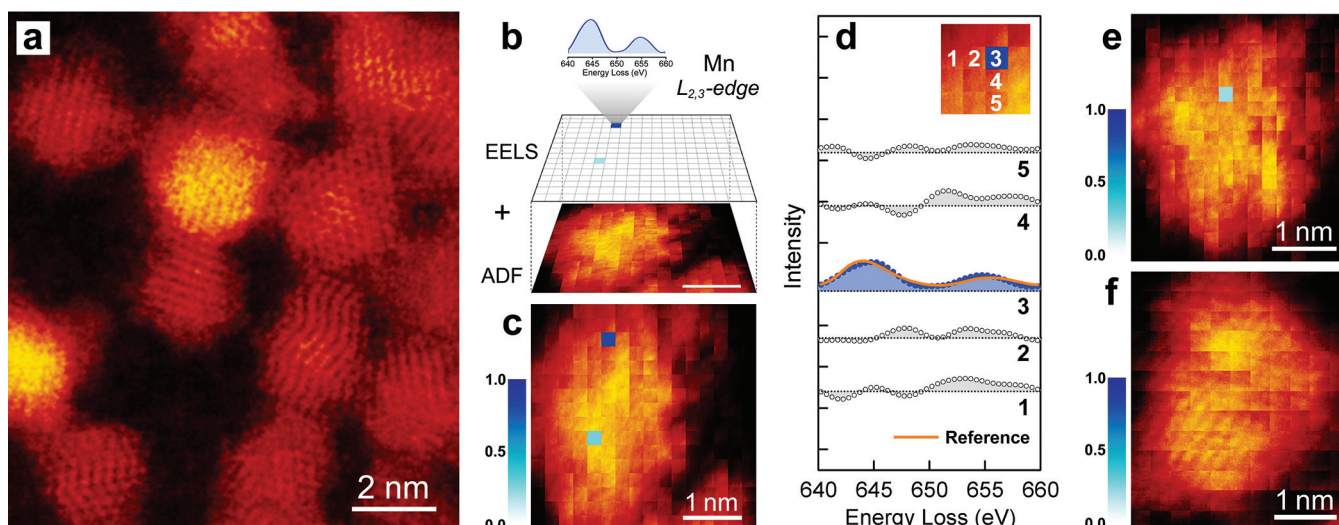
Figure 1. (a) Atomic-resolution ADF-STEM image of Mn-doped ZnSe nanocrystals (Sample 1) suspended on an ultrathin amorphous carbon film. Periodic arrangements of the atomic columns along different crystallographic directions are seen. The image has been low-pass filtered to remove scan noise. (b) The extracted core-level EELS map (shown as pixels on a grid) for the Mn $L_{2,3}$-edge along with the corresponding ADF-STEM image of a Mn-doped ZnSe nanocrystal (Sample 2). The energy loss spectrum for one of the pixels where Mn was detected is shown. The characteristic double-peaked EELS spectrum for the Mn $L_{2,3}$-edge is seen. (c) Overlap of the Mn $L_{2,3}$-edge intensity map and the ADF-STEM image, both shown in (b). The atomic-resolution in the ADF-STEM image is lost in this scanning mode. (d) Measured EELS Mn $L_{2,3}$-edge from five pixels from the map shown in (c). A low-pass filter was applied to the EELS spectra to remove instrumental noise. A reference EELS Mn $L_{2,3}$-edge is also shown (orange curve). (e) EELS Mn $L_{2,3}$-edge intensity map overlapped with the ADF-STEM image from a different Mn-doped ZnSe nanocrystal (Sample 2). (f) An example of the EELS Mn $L_{2,3}$-edge intensity map overlapped with the ADF-STEM image from an undoped ZnSe nanocrystal (Sample 3) showing no Mn EELS signals, as expected.

contrast with the surrounding semiconductor atoms to ensure its visibility.[24,25] Other methods are needed for the many cases when this condition is not satisfied, including doped semiconductor nanocrystals.

The combination of STEM and electron energy loss spectroscopy (EELS) has previously proven very effective for compositional analysis at the atomic-scale and for measuring local electronic and optical properties of materials.[26] For imaging of buried dopants, it has an additional advantage. Unlike standard high-resolution ADF-STEM imaging, where the visibility of the dopant is related to the small change in the scattered-electron signal when the beam scans between an atomic column with an impurity and one without, EELS mapping is based on detecting a characteristic core-edge electron-energy-loss signal from the dopant compared to an essentially zero background. Consequently, single-atom sensitivity with EELS has already been demonstrated.[27−30] However, in only one example[28] was the detected atom buried in a solid (an oxide). Further, in that case the detected atom (La) had sufficient Z-contrast that its exact position had already been determined with standard ADF-STEM imaging. Therefore, it remains an open question whether individual, low-Z-contrast, dopant atoms that are buried inside a semiconductor can be convincingly detected when they are invisible to standard imaging techniques.

To examine this question we used Mn-doped ZnSe nanocrystals as a test system. Mn is a convenient impurity because it is expected to be invisible to standard ADF-STEM imaging in this host. We also know due to extensive previous characterization[11,31] (e.g. with electron paramagnetic resonance measurements) that the Mn atoms in these samples are incorporated as substitutional impurities inside the nanocrystals and not simply bound to their surfaces.

We measured EELS of the Mn $L_{2,3}$-edge while the STEM probe scanned across an individual nanocrystal. The Mn $L_{2,3}$-edge exhibits an identifiable double-peaked spectrum and is the only EELS feature between 640 and 660 eV in our samples.[32] Thus, atomic columns with (without) a Mn should appear bright (dark) when the EELS signal from this energy range is used for imaging.

The data were collected with a Nion aberration-corrected Ultra-STEM operated at 100 keV. The microscope was equipped with a cold-field-emission gun, an ADF detector, and a parallel EELS spectrometer. With a 30 mrad convergent beam corrected for spherical aberrations of the objective lens up to fifth order, a STEM probe with a diameter of 1.2 Å was obtained. The incident beam current was measured to be 150−200 pA. Such a high current was necessary to detect the Mn $L_{2,3}$-edge while scanning the probe.[33] From separate measurements, we confirmed that this current was below the sample damage threshold. See Supporting Information for further details.

Three ZnSe samples were examined: (1) 2.9 nm diameter nanocrystals with 0.13 atom % incorporated Mn (an average of 0.7 ± 0.14 Mn per nanocrystal), (2) 3.7 nm nanocrystals with 0.58 atom % Mn (6.2 ± 1.5 Mn per nanocrystal), and (3) a reference sample of ∼2 nm undoped nanocrystals. For imaging experiments, nanocrystals were drop-cast from dispersions onto copper microscopy grids coated with thin amorphous carbon. Before loading each specimen into the STEM, it was exposed to acetone vapor and then heated under vacuum at 130 °C to remove ligands from the nanocrystal surface.

Figure 1a shows a typical high-resolution ADF-STEM image for Sample 1. Atomic columns within individual nanocrystals can be clearly seen. From such an image, we then selected one of the nanocrystals and simultaneously collected an ADF-STEM image and an EELS map. For this, the STEM probe was
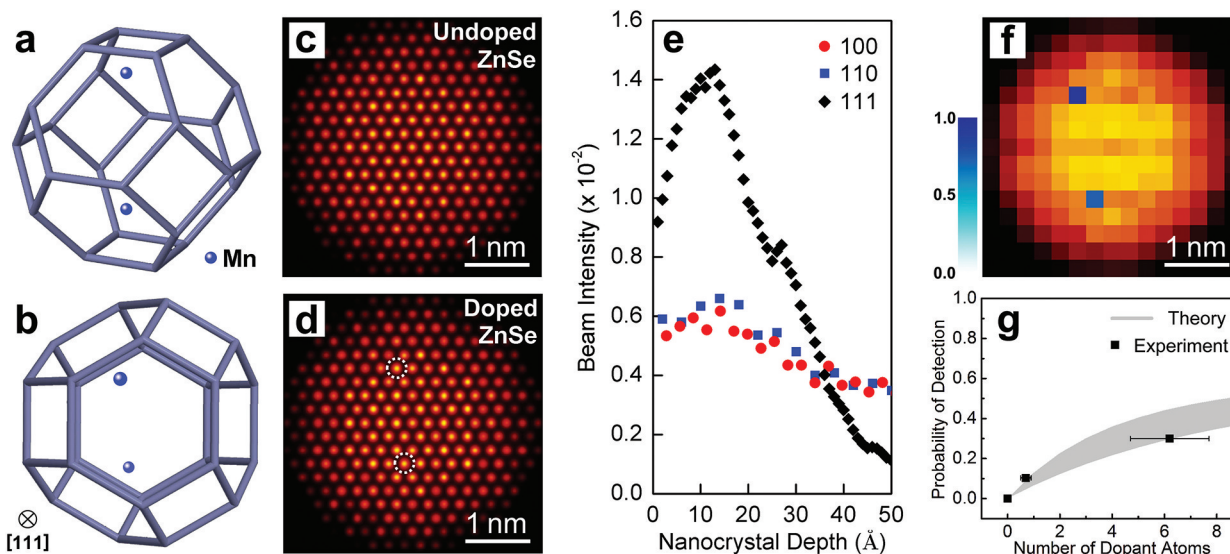
Figure 2. (a) Outline of a faceted 4 nm ZnSe nanocrystal with two Mn dopants inside. (b) The structure in (a) viewed along the [111] crystallographic direction. The upper dopant is 1.3 nm below the top surface of the nanocrystal and the lower one is 2.9 nm below. (c) Simulated high-resolution ADF-STEM image of a 4 nm undoped ZnSe nanocrystal viewed along the [111] crystallographic direction. (d) Simulated high-resolution ADF-STEM image of a 4 nm ZnSe nanocrystal with two Mn dopants as in (b). The circles indicate the atomic columns where the Mn are located. Even without the presence of noise in the simulation, the contrast is insufficient to observe the Mn. (e) Calculated STEM electron beam intensity at the atomic column as the beam propagates along the [100], [110], and [111] crystallographic directions. (f) Overlap of the simulated normalized Mn $L_{2,3}$-edge intensity map with the ADF-STEM image for the case in (d) under the experimental conditions used in Figure 1c. (g) Calculated probability of finding a nanocrystal with at least one detected Mn dopant in the ZnSe nanocrystal using core-level EELS under the experimental conditions. Experimental measurements (Samples 1 and 2) are shown for comparison.

scanned across the nanocrystal with ∼2.5 Å steps and a 0.2 s dwell time. To reduce the possibility of sample damage, the probe was moved during the dwell in 16 × 16 steps within each 2.5 × 2.5 Å^2 pixel. After the full scan, each pixel in the raw EELS map contains an energy loss spectrum in the energy range sensitive to Mn.

As expected for such an experiment, the raw data contain noise (both statistical and instrumental) and further signal processing was performed. First, for each pixel the background was subtracted and the instrumental noise was removed using a low-pass filter. Each result was then quantitatively compared to a reference spectrum for the Mn $L_{2,3}$-edge collected from bulk crystalline PtMn with the same apparatus. Specifically, a least-squares algorithm scaled the reference spectrum to see if the nanocrystal data could be fit. Thus, for each pixel two relevant parameters were obtained: the goodness-of-fit, G, which quantifies how closely the data matches the characteristic double-peaked spectrum of the Mn $L_{2,3}$-edge, and the scaling factor, S, which is related to the intensity of the signal in this double-peaked region. A two-dimensional EELS map was then generated from $M(i,j) = G(i,j)S(i,j)$, where i and j are integers that label the pixels. To eliminate any remaining artifacts, we defined threshold values for $G(i,j)$ and $S(i,j)$ that needed to be exceeded. A positive Mn signal in our map required $G(i,j)$ to be larger than any goodness-of-fit obtained when we performed the same analysis on undoped ZnSe nanocrystals. $S(i,j)$ was required to be 2.5 times larger than the noise, defined as the average of $|S(i,j)|$. See the Supporting Information and Figure S1 for details.

Figure 1b shows an example of $M(i,j)$. It represents the resolved intensity map for the Mn $L_{2,3}$-edge and can be used to locate the dopants in the nanocrystal when overlapped with the ADF-STEM image (Figure 1c). If we compare EELS spectra for different spots (Figure 1d), only the bright pixel in $M(i,j)$

exhibits the double-peaked shape seen in the reference. When the same overall analysis was repeated on a number of individual doped nanocrystals, similar results were observed (e.g., see Figure 1e). However, our procedure did not detect any Mn in any of the undoped nanocrystals (Figure 1f) that were analyzed.

We also compared these experimental results with simulations. We utilized the Multislice code[34] to describe the electron-beam propagation through the material. Multislice uses the frozen-phonon approximation to model atomic thermal vibrations.[35] Using the experimental beam parameters, the 1.2 Å STEM probe was modeled (Figure S2 in the Supporting Information). We then combined this with a simple quantum-mechanical description of the core-level electronic transitions of Mn. Thus, both the ADF-STEM images and EELS map could be simulated.

Figure 2 summarizes the results. A faceted 4 nm ZnSe nanocrystal with the zinc-blende crystal structure was first constructed (Figure 2a,b, and Figure S3 in the Supporting Information). High-resolution ADF-STEM images of this nanocrystal were then generated with the model. The result for an undoped nanocrystal viewed along the [111] crystallographic direction is shown in Figure 2c. The same nanocrystal with two Mn atoms, located 1.3 and 2.9 nm below the top surface (or beam entry surface) of the nanocrystal, appears in Figure 2d. Since the Z-contrast between the dopant ($Z_{Mn} = 25$) and the host atoms ($Z_{Zn} = 30$) is small, the Mn atoms are not visible in the simulated ADF-STEM images, as expected (see also Figure S4 in the Supporting Information). Note that the Mn atoms are invisible even in this simulation where the statistical and instrumental noise that would be present in a real experiment is absent.

To estimate the expected EELS signal for the Mn, the local beam intensity must be multiplied by the probability that a

relevant electronic transition in Mn will occur. Electrons are excited from an initial core-level state, $|i\rangle = |2p_{1/2}\rangle$ or $|2p_{3/2}\rangle$, to a final state, $|f\rangle$, which is near or above the Fermi level. Because the 2p core-levels of Mn are highly localized (with a radius, r_{2p}, of 0.21 Å[36]), the EELS signal will originate from a very small volume. The Mn EELS map can be simulated according to $M_{sim}(i,j) = CI_{2p}(i,j)$, where $I_{2p}(i,j)$ is the portion of the incident electron beam that has a finite probability of exciting an electron from the 2p orbitals of the Mn. It can be well approximated by the intensity of the beam that passes through the spherical volume around the Mn with $r < r_{2p}$ (see Supporting Information and Figure S5). C is a constant that includes the transition cross-section and experimental parameters related to the microscope.

Our Multislice simulations also show that the intensity of the electron beam depends on the crystal orientation. In Figure 2e, the electron beam is first focused on the top surface of the nanocrystal. The beam intensity is then plotted as it propagates through the ZnSe crystal for three main crystallographic orientations, [100], [110], and [111]. The results indicate that the EELS signal from the Mn should be stronger if the nanocrystal is oriented along the [111] direction. The arrangement of the atoms for this direction causes stronger beam channeling along the atomic column. This leads to a higher concentration of probe electrons near the atomic nuclei and consequently, a higher rate of core-level electronic transitions. In addition, for the [111] direction, the intensity is maximized at a depth of ~10 Å. Thus, the technique is more sensitive to buried dopants than those at the surface.

The simulated EELS map for the 4 nm, [111]-oriented ZnSe nanocrystal with two dopant atoms (as depicted in Figure 2b) is shown in Figure 2f. The EELS map is overlaid with the simulated ADF-STEM image from Figure 2d but with the resolution reduced to match the conditions in Figure 1c. The simulation confirms the detectability of the Mn with the STEM-EELS approach and reproduces the experimental results. In particular, a detailed analysis (see Supporting Information) indicates that when the incident STEM probe is located more than 1 Å from the center of the atomic column containing the dopant in the ZnSe nanocrystal, the portion of the beam that overlaps the 2p core-levels is practically negligible (Figure S6 in the Supporting Information). This explains why, even without experimental noise, the EELS maps show only one pixel per Mn.

Finally, we used our model to estimate the detection probability. Since the dopant can be located at many different lattice sites inside the nanocrystal, the frequency of detection could be analyzed statistically. The probability of finding a nanocrystal with at least one detected dopant can be expressed as $P = 1 - (1 - p_S)^N$, where p_S is the probability of detecting the dopant and N is the number of dopants per nanocrystal. It should be noted that since the beam propagation is different along different crystallographic directions, the probability p_S also varies with direction. Figure 2g shows the estimated probability P including uncertainties in the estimation of p_S and the corresponding weights of all possible crystallographic directions (see Supporting Information and Figure S7). The results are in good agreement with our experimental observations for the two doped samples.

Since in these samples the Mn atoms are known to be inside the nanocrystals and not simply on their surfaces,[11,31] these results indicate that STEM-EELS presents a technique for imaging individual dopants in semiconductor nanostructures. It should be broadly applicable to the many impurities that have a suitable EELS edge, typically those with an energy less than 1 keV.[33] This includes elements from Li ($Z_{Li} = 2$) to Cu ($Z_{Cu} = 29$) with strong EELS signals for the K- or $L_{2,3}$-edges, elements from Kr ($Z_{Kr} = 36$) to Ru ($Z_{Ru} = 44$) with a strong $M_{4,5}$-edge between 80 and 300 eV, and elements from Cs ($Z_{Cs} = 55$) to Yb ($Z_{Yb} = 70$) with strong $M_{4,5}$- or $N_{4,5}$-edges. The sensitivity of the approach can be improved even further for dopants that have a higher cross-section for core-level excitations or if the host semiconductor can sustain a higher electron dose from the scanning probe without damage. This suggests that the use of an aberration-corrected STEM with a high-brightness gun and low beam-accelerating voltage will be preferable. In addition to revealing the location of previously invisible dopants, which can aid in the fabrication and characterization of doped nanostructures, this technique can potentially allow other studies, such as the analysis of dopant diffusion.

■ ASSOCIATED CONTENT

Ⓢ Supporting Information
Experimental methods and simulation details. This material is available free of charge via the Internet at http://pubs.acs.org.

■ AUTHOR INFORMATION

Corresponding Author
*E-mail: (K.A.M.) mkhoyan@umn.edu; (D.J.N.) dnorris@ethz.ch.

■ ACKNOWLEDGMENTS

■ REFERENCES

(1) Asenov, A.; Brown, A. R.; Davies, J. H.; Kaya, S.; Slavcheva, G. *IEEE Trans. Electron Devices* **2003**, *50*, 1837.

(2) Koenraad, P. M.; Flatté, M. E. *Nat. Mater.* **2011**, *10*, 91.

(3) Hoeneise, B.; Mead, C. A. *Solid-State Electron.* **1972**, *15*, 819.

(4) Ohnishi, T.; Shibuya, K.; Yamamoto, T.; Lippmaa, M. *J. Appl. Phys.* **2008**, *103*, 103703.

(5) Spinelli, A.; Torija, M. A.; Liu, C.; Jan, C.; Leighton, C. *Phys. Rev. B* **2010**, *81*, 155110.

(6) Klimov, V. I. *Nanocrystal Quantum Dots*, 2nd ed.; CRC Press: Boca Raton, FL, 2010.

(7) Klimov, V. I.; Ivanov, S. A.; Nanda, J.; Achermann, M.; Bezel, I.; McGuire, J. A.; Piryatinski, A. *Nature* **2007**, *447*, 441.

(8) Michalet, X.; Pinaud, F. F.; Bentolila, L. A.; Tsay, J. M.; Doose, S.; Li, J. J.; Sundaresan, G.; Wu, A. M.; Gambhir, S. S.; Weiss, S. *Science* **2005**, *307*, 538.

(9) Gur, I.; Fromer, N. A.; Geier, M. L.; Alivisatos, A. P. *Science* **2005**, *310*, 462.

(10) Hoffman, D. M.; Meyer, B. K.; Ekimov, A. I.; Merkulov, I. A.; Efros, Al. L.; Rosen, M.; Couino, G.; Gacoin, T.; Boilot, J. P. *Solid State Commun.* **2000**, *114*, 547.

(11) Norris, D. J.; Yao, N.; Charnock, F. T.; Kennedy, T. A. *Nano Lett.* **2001**, *1*, 3.

(12) Bussian, D. A.; Crooker, S. A.; Yin, M.; Brynda, M.; Efros, Al. L.; Klimov, V. I. *Nat. Mater.* **2009**, *8*, 35.

(13) Beaulac, R.; Schneider, L.; Archer, P. I.; Bacher, G.; Gamelin, D. R. *Science* **2009**, *325*, 973.

(14) Bryan, J. D.; Gamelin, D. R. *Prog. Inorg. Chem.* **2005**, *54*, 47.

(15) Norris, D. J.; Efros, Al. L.; Erwin, S. C. *Science* **2008**, *319*, 1776.

(16) Mocatta, D.; Cohen, G.; Schattner, J.; Millo, O.; Rabani, E.; Banin, U. *Science* **2011**, *332*, 77.

(17) Perea, D. E.; Allen, J. E.; May, S. J.; Wessels, B. W.; Seidman, D. N.; Lauhon, L. J. *Nano Lett.* **2006**, *6*, 181.

(18) Pennycook, S. J.; Boatner, L. A. *Nature* **1988**, *336*, 565.

(19) Batson, P. E.; Dellby, N.; Krivanek, O. L. *Nature* **2002**, *418*, 617.

(20) Nellist, P. D.; Chisholm, M. F.; Dellby, N.; Krivanek, O. L.; Murfitt, M. F.; Szilagyi, Z. S.; Lupini, A. R.; Borisevich, A.; Sides, W. H.; Pennycook, S. J. *Science* **2004**, *305*, 1741.

(21) Voyles, P. M.; Muller, D. A.; Grazul, J. L.; Citrin, P. H.; Gossmann, H. J. L. *Nature* **2002**, *416*, 826.

(22) Shibata, N.; Findlay, S. D.; Azuma, S.; Mizoguchi, T.; Yamamoto, T.; Ikuhara, Y. *Nat. Mater.* **2009**, *8*, 654.

(23) Krivanek, O. L.; Chisholm, M. F.; Nicolosi, V.; Pennycook, T. J.; Corbin, G. J.; Dellby, N.; Murfitt, M. F.; Own, C. S.; Szilagyi, Z. S.; Oxley, M. P.; Pantelides, S. T.; Pennycook, S. J. *Nature* **2010**, *464*, 571.

(24) Voyles, P. M.; Muller, D. A.; Kirkland, E. J. *Microsc. Microanal.* **2004**, *10*, 291.

(25) Mittal, A.; Mkhoyan, K. A. *Ultramicroscopy* **2011**, *111*, 1101.

(26) Daniels, J.; Festenberg, C. V.; Raether, H.; Zeppenfeld, K. Optical Constants of Solids by Electron Spectroscopy. In *Springer Tracts in Modern Physics*; Hohler, G., Ed.; Springer-Verlag: Berlin, 1970; Vol. *54*, p 77.

(27) Suenaga, K.; Tence, T.; Mory, C.; Colliex, C.; Kato, H.; Okazaki, T.; Shinohara, H.; Hirahara, K.; Bandow, S.; Iijima, S. *Science* **2000**, *290*, 2280.

(28) Varela, M.; Findlay, S. D.; Lupini, A. R.; Christen, H. M.; Borisevich, A. Y.; Dellby, N.; Krivanek, O. L.; Nellist, P. D.; Oxley, M. P.; Allen, L. J.; Pennycook, S. J. *Phys. Rev. Lett.* **2004**, *92*, 095502.

(29) Suenaga, K.; Sato, Y.; Liu, Z.; Kataura, H.; Okazaki, T.; Kimoto, K.; Sawada, H.; Sasaki, T.; Omoto, K.; Tomita, T.; Kaneyama, T.; Kondo, Y. *Nature Chem.* **2009**, *1*, 415.

(30) Suenaga, K.; Koshino, M. *Nature* **2010**, *468*, 1088.

(31) Zu, L.; Wills, A. W.; Kennedy, T. A.; Glaser, E. R.; Norris, D. J. *J. Phys. Chem. C* **2010**, *114*, 21969.

(32) Egerton, R. F. *Electron Energy Loss Spectroscopy in the Electron Microscope*, 2nd ed.; Plenum Press: New York, 1996.

(33) Krivanek, O. L.; Dellby, N.; Murfitt, M. F.; Chisholm, M. F.; Pennycook, T. J.; Suenaga, K.; Nicolosi, V. *Ultramicroscopy* **2010**, *110*, 935.

(34) Kirkland, E. J. *Advanced Computing in Electron Microscopy*, 2nd ed.; Springer: New York, 2010.

(35) Loane, R. F.; Xu, P. R.; Silcox, J. *Acta Crystallogr.* **1991**, *A 47*, 267.

(36) Cohen-Tannoudji, C.; Diu, B.; Laloë, F. *Quantum Mechanics*; John Wiley & Sons: New York, 1977.